

Article

# A Comparative Study on Permanent Mold Cast and Powder Thixoforming 6061 Aluminum Alloy and SiC<sub>p</sub>/6061Al Composite: Microstructures and Mechanical Properties

Xuezheng Zhang, Tijun Chen \*, He Qin and Chong Wang

State Key Laboratory of Advanced Processing and Recycling of Nonferrous Metals, Lanzhou University of Technology, Lanzhou 730050, China; zhangxz1991@163.com (X.Z.); qinhe19900927@126.com (H.Q.); wangchong19890329@126.com (C.W.)

\* Correspondence: chentj@lut.cn; Tel.: +86-931-2976-573; Fax: +86-931-2976-578

Academic Editor: Mark Whittaker

Received: 24 April 2016; Accepted: 18 May 2016; Published: 24 May 2016

**Abstract:** Microstructural and mechanical characterization of 10 vol% SiC particles (SiC<sub>p</sub>) reinforced 6061 Al-based composite fabricated by powder thixoforming (PTF) was investigated in comparison with the PTF and permanent mold cast (PMC) 6061 monolithic alloys. The results reveal that the microstructure of the PMC alloy consists of coarse and equiaxed  $\alpha$  dendrites and interdendritic net-like eutectic phases. However, the microstructure of the PTF composite, similar to that of the PTF alloy, consists of near-spheroidal primary particles and intergranular secondarily solidified structures except SiC<sub>p</sub>, which are distributed in the secondarily solidified structures. The eutectics amount in the PTF materials is distinctly lower than that in the PMC alloy, and the microstructures of the former materials are quite compact while that of the latter alloy is porous. Therefore, the PTF alloy shows better tensile properties than the PMC alloy. Owing to the existence of the SiC reinforcing particles, the PTF composite attains an ultimate tensile strength and yield strength of 230 MPa and 128 MPa, representing an enhancement of 27.8% and 29.3% than those (180 MPa and 99 MPa) of the PTF alloy. A modified model based on three strengthening mechanisms was proposed to calculate the yield strength of the PTF composite. The obtained theoretical results were quite consistent with the experimental data.

**Keywords:** powder thixoforming; permanent mould cast; SiC<sub>p</sub>/6061Al composite; microstructure; tensile properties; strengthening mechanisms

## 1. Introduction

Developing low density, high specific stiffness and super dimensional stability materials have always attracted considerable attention for aerospace and automobile industrial applications [1,2]. Aluminum matrix composites (AMCs) reinforced with ceramic particles are particularly attractive because of their superior strength, stiffness and wear resistance. In addition, they have excellent isotropic mechanical and physical properties both at ambient and elevated temperatures in comparison with the conventional monolithic alloys [1]. One main problem still always plagues the incorporation of micro-size ceramic particles into the aluminum matrix: the high clustering tendency of micro-particles [3]. Numerous methods have been developed to overcome this problem such as melt stirring [2,3], ultrasonic dispersion [4], squeeze casting [5,6] and powder metallurgy [7,8]. Among the various processing techniques, powder metallurgy has prominent advantages such as flexible design of the constituents and uniform distribution of ceramic particles [8], but the as-obtained composites inevitably comprise numerous voids, though some advanced sintering techniques are

employed. Besides, it is not suitable to apply powder metallurgy to produce parts with large sizes or complex shapes [7]. Thixoforming, a promising metal-forming technology that can markedly diminish voids, has been introduced to be integrated with powder metallurgy and thus a novel technology called PTF is developed. The PTF not only retains the advantages of powder metallurgy, but also inherits the merits of compact microstructure and being available for producing large-sized and complicated components of the thixoforming. Unfortunately, the focus of the existing research into PTF was mainly on the microstructure evolution during partial remelting and mechanical properties of aluminum matrix alloys [9–11]. Only a few studies involved composites fabricated by PTF, and they concentrated on the effects brought out by solution treatment [12] or failed to consider the corresponding mechanical properties [13].

The main purpose of this study is to highlight the advantage of this novel technology and elucidate the strengthening mechanisms of  $\text{SiC}_p$  in the PTF- $\text{SiC}_p/6061\text{Al}$  composite. To achieve this goal, several 10 vol% of  $6.94\ \mu\text{m}$   $\text{SiC}_p$  reinforced 6061 Al-based composite samples were prepared using PTF, and the resulting microstructure, mechanical properties and fracture behavior were investigated in detail in comparison with those of the matrix alloys fabricated by PMC and PTF, respectively. A modified model on the basis of three strengthening mechanisms was proposed to calculate the yield strength of this composite. The obtained theoretical results were found to be quite consistent with the experimental data.

## 2. Materials and Methods

### 2.1. Fabrication PMC of 6061 Alloy

The PMC-6061 alloy employed in this work was prepared by pure Al, Mg, Cu and Al-20Si master alloy (all of them were provided by Changfeng factory, Lanzhou, China) and the resulting alloy possessed a nominal composition of Al-1.0Mg-0.6Si-0.3Cu (wt%). A schematic illustration of the PMC process is presented in Figure 1. First, a quantity of the master alloy and pure metals was melted in a resistance furnace at 1023 K. Degassing was then conducted at 1003 K by adding 1.5 wt%  $\text{C}_2\text{Cl}_6$  (Kejia Chemical Company, Ningbo, China) into the melt. The melt was held for 5 min and ultimately injected into a permanent mold (Changfeng factory, Lanzhou, China) with diameters of 50 mm and lengths of 500 mm. Some specimen cakes with diameters of 50 mm and lengths of 15 mm were cut from the cast rods.

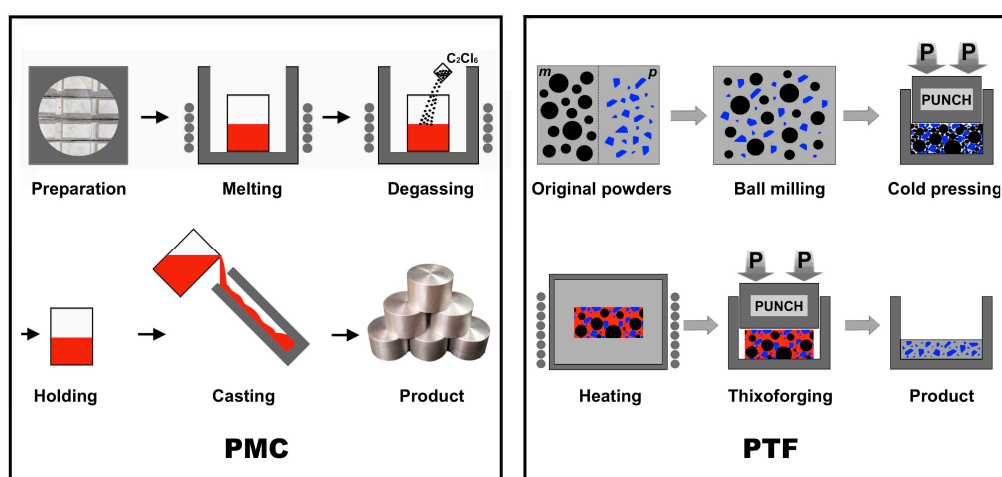


**Figure 1.** Schematic illustration of the PMC and PTF process ( $m$ : matrix;  $p$ :  $\text{SiC}_p$ ).

### 2.2. Fabrication PTF of $\text{SiC}_p/6061$ Composite and 6061 Alloy

The raw materials used in the fabrication of  $\text{SiC}_p/6061$  composite and 6061 alloy were atomized 6061 alloy powders and pre-oxidized  $\text{SiC}$  particles with an average size of  $17.91\ \mu\text{m}$  and  $6.94\ \mu\text{m}$ ,

respectively. For comparison, the schematic diagram of the PTF process for SiC<sub>p</sub>/6061 composite is also presented in Figure 1. First, 6061 alloy powders were mixed with 10 vol% SiC<sub>p</sub> and the resulting powders were subjected to ball milling in an ND7-21 planetary ball-milling machine (Nanjing Laibu Technology Industry Co., Ltd., Nanjing, China) at a mixing time, rotation speed and ball-to-powder weight ratio of 40 min, 100 rpm and 5:1, respectively. The resultant powder mixture was then cold pressed into a specimen with 50 mm in diameter and 15 mm thickness under a pressure of 150 MPa. Based on the results of an existing research [14], one specimen was heated in a resistance furnace at 933 K for 90 min. Then the heated specimen was quickly put into a forging mold (Changfeng factory, Lanzhou, China) with a cavity 55 mm in diameter and 45 mm deep, and finally thixoformed under an optimized pressure of 160 MPa. Repeating the above experimental procedure, several PTF-SiC<sub>p</sub>/6061Al composite cakes can be obtained. The fabrication process of the PTF-6061 alloy was similar to that of the PTF-SiC<sub>p</sub>/6061Al composite with the exception of ball milling.

### 2.3. Material Characterization

Metallographic specimens 10 mm in diameter and 10 mm long were machined from the central region of a cake specimen, and then ground, finished, polished and etched using an aqueous solution of 10 vol% NaOH (Kejia Chemical Company, Ningbo, China). Subsequently, the specimens were observed on a MeF3 optical microscope (OM; Nikon Instruments, Shanghai, China) and a QUANTA FEG 450 scanning electron microscope (SEM; FEI, Hillsboro, TX, USA) equipped with an energy dispersive spectroscope (EDS). The estimation of the shape factor and volume fraction of the primary particles in the PTF materials as well as the grain size of these three materials were carried out by Image-Pro Plus 6.0 software (Media Cybernetics Company, Silver Spring, MD, USA) utilizing the OM images randomly captured in minimum ten different locations for each specimen. Similar methods were also used to calculate the eutectics fraction of these three materials. The area ratio of the eutectic phases to the whole ones was taken as the eutectics fraction. In attempt to verify the detailed fracture mechanisms of these materials, some typical fracture surfaces and their corresponding side views were observed on the SEM and OM. The density of the specimens was measured by the Archimedes method so as to calculate the porosity of the specimens.

### 2.4. Tensile Testing

The mechanical properties of these three materials were evaluated by tensile testing conducted at room temperature (about 293 K) on a WDW-100D universal material testing machine (Jinan HengXu Testing Machine Technology Co., Ltd., Jinan, China) with a loading velocity of  $5 \times 10^{-3}$  m/s. The tensile bars with a gauge length of 10 mm and a cross-section of 2.5 mm long and 1.5 mm wide were cut from the central part of a specimen cake. The average of minimum five tests was taken as the tensile properties of each material.

## 3. Results and Discussion

### 3.1. Microstructural Analysis

Figure 2 shows the microstructures of the PMC-6061 alloy and PTF-6061 alloy. The microstructure of the PMC-6061 alloy is mainly composed of coarse and equiaxed  $\alpha$  dendrites with an average size of 90.01  $\mu\text{m}$  and interdendritic net-like eutectic phases (Figure 2a). The eutectic phases of  $\alpha$ -Al, Mg<sub>2</sub>Si and Si [15] are distributed in a skeleton shape along the grain boundaries (Figure 2b). As shown in Figure 2c, the microstructure of the PTF-6061 alloy consists of near-spheroidal primary  $\alpha$ -Al particles with an average size of only 16.83  $\mu\text{m}$  and intergranular secondarily solidified structures. The secondarily solidified structures are comprised of small spheroidal secondarily primary  $\alpha$  grains (to differentiate from the primary  $\alpha$ -Al particles, the primary  $\alpha$  grains solidified from the liquid phase in a semi-solid state are named as secondarily primary  $\alpha$  grains) and intergranular eutectic structures (Figure 2d). Similar to the PMC alloy, the eutectic phases are also distributed in skeleton shapes along the grain

boundaries (Figure 2e). Based on the phase constituents and microstructure of the PTF alloy as discussed above, the secondary solidification process can be divided into three stages. First, due to the presence of the primary  $\alpha$ -Al particles, the secondary primary  $\alpha$ -Al particles grow directly on the surfaces of the primary particles without nucleation [16], resulting in the formation of annular or serrated structure attachments to the primary  $\alpha$ -Al particles (marked by arrows A in Figure 2f). Then, nucleation appears in the liquid phase far away from the primary particles, resulting in the generation of numerous small globular  $\alpha$  grains (marked by arrows B in Figure 2f). Finally, the solidification is completed by the eutectic reaction of  $L \rightarrow \alpha\text{-Al} + \text{Mg}_2\text{Si} + \text{Si}$ . Overall, the microstructures under these two forming techniques are distinctly different. The microstructure of the PMC-6061 alloy is composed of coarse and equiaxed  $\alpha$  dendrites with an average size of 90.01  $\mu\text{m}$  and interdendritic net-like eutectic phases, while that of the PTF-6061 alloy consists of near-spheroidal primary  $\alpha$ -Al particles with an average size of only 16.83  $\mu\text{m}$  and intergranular secondarily solidified structures.

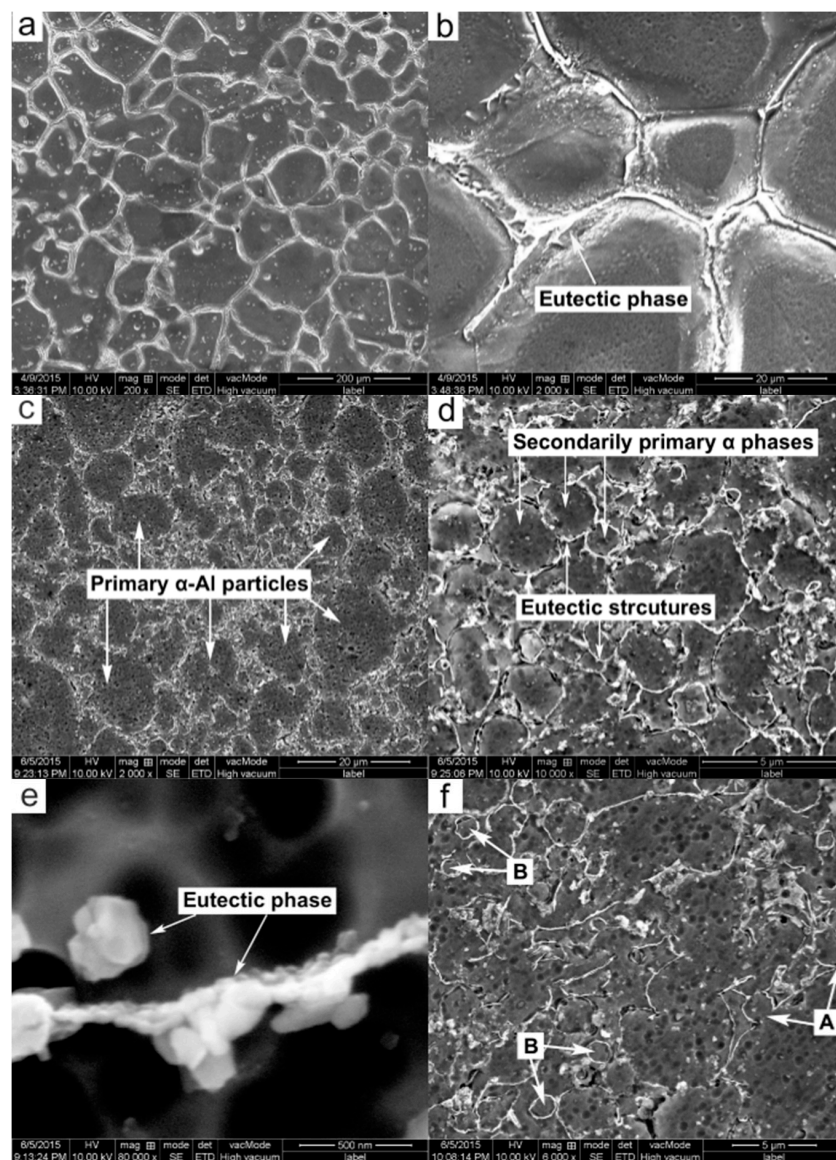
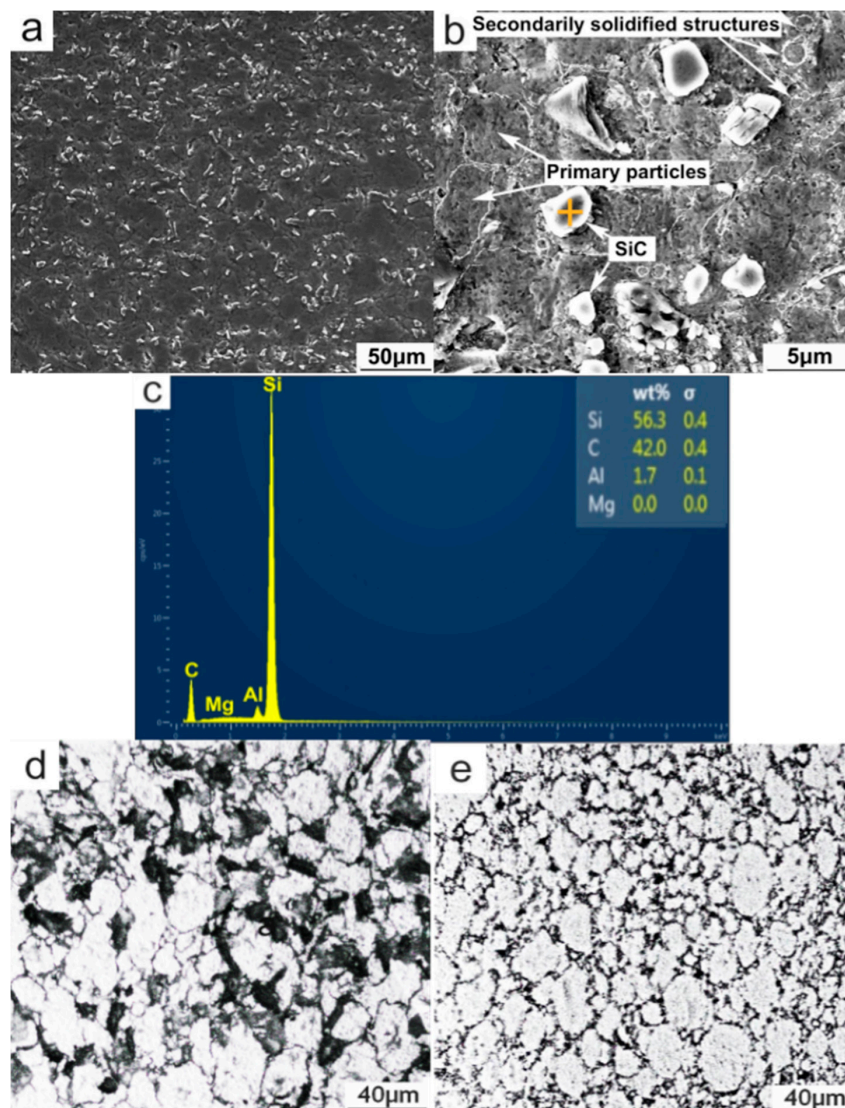


Figure 2. SEM images of: (a,b) PMC-6061 alloy; (c–f) PTF-6061 alloy.

For the PTF-SiC<sub>p</sub>/6061 Al composite, SiC reinforcements are uniformly distributed in the matrix under the low-magnification SEM image (Figure 3a). The microstructure, similar to that of the PTF-6061 alloy, also consists of near-spheroidal primary particles and intergranular secondarily solidified

structures except the  $\text{SiC}_p$ , which distribute in the secondarily solidified structures (Figure 3b,c). The statistics indicate that the shape factor and volume fraction of the primary particles in the PTF composite attain values of 2.3% and 89.3%, respectively (Figure 3d), which are higher than those (1.8% and 87.6%) in the PTF alloy (Figure 3e), disclosing a more irregular morphology of the primary particles (if the particles are perfectly spherical, the shape factor has a value of 1; it increases for less spherical particles [17]) and fewer secondarily solidified structures in the PTF composite. Both of the PTF materials were reheated at the same temperature (933 K) during partial remelting. However, the existence of  $\text{SiC}_p$  would impede the heat transfer from the edge to the center of the semisolid ingot due to its low thermal conductivity and the microstructural evolution rate of the PTF composite is thereby delayed. This accounts for the higher volume fraction of primary particles in the PTF composite. In accordance with a report by Chen *et al.* [11], the microstructural evolution of 6061 alloy powders during partial remelting was divided into three stages:

- the initial coarsening
- structure separation and spheroidization
- final coarsening



**Figure 3.** (a,b) SEM images of PTF- $\text{SiC}_p$ /6061Al composite; (c) EDS result of the cross in Figure 3b proving the presence of  $\text{SiC}_p$ ; (d) OM micrograph of PTF- $\text{SiC}_p$ /6061Al composite; (e) OM micrograph of PTF-6061 alloy.

It can be expected that the spheroidization stage of the PTF composite should lag behind that of the PTF alloy owing to the delayed heat transferring in the former material. That is, when all of the primary particles in the PTF alloy were fully spheroidized and entered into the final stage, the spheroidization stage in the PTF composite may just occur because of its delayed evolution rate. Therefore, the primary particles of the PTF composite are less spherical, *i.e.*, its shape factor is higher than that of the PTF alloy. The quantitative examination also indicates that the average size (16.51  $\mu\text{m}$ ) of the primary particles of the PTF composite is slightly smaller than that of the PTF alloy (comparing Figure 3d,e). With respect to the  $\text{SiC}_p$ , two main factors influence the semisolid microstructure prior to thixoforming. First, as mentioned above, the presence of  $\text{SiC}_p$  delays the microstructural evolution rate. Therefore, the coarsening of the composite from Ostwald ripening as well as the coalescence of the nearby primary particles is delayed. Secondly, the  $\text{SiC}_p$  located in the liquid phase between the primary particles would hinder the coalescence of the neighboring primary particles and play an obstacle role in atom diffusion. Under these circumstances, the size of the primary particles in the PTF composite is slightly smaller than that in the PTF alloy. In conclusion, the microstructure of the PTF composite differs from that of the PTF alloy. The primary particles are more irregular and the amount of secondarily solidified structures is less than those of the PTF alloy because of the delayed microstructural evolution rate during partial remelting. Besides, the size of the primary particles is slightly smaller than that in the PTF alloy due to the delayed microstructural evolution rate as well as the pinning effect of  $\text{SiC}_p$  against the coalescence of the nearby primary particles.

In an attempt to examine the differences in the eutectics amount of these three materials, the statistical measure was utilized in the Figure 2b,c,f and Figure 3b with the same magnification. Comparison with Figure 2b,c indicates that the eutectics fraction of the PMC alloy is up to 6.7%, which is obviously higher than that of the PTF alloy (3.2%). Nevertheless, comparison with Figures 2f and 3b discloses that the eutectics fraction of the PTF alloy is slightly higher than that of the PTF composite (2.4%). Results from the EDS analysis of the compositions of  $\alpha$ -Al phase in these three materials also confirm this viewpoint. As shown in Table 1, the Mg and Si concentrations in these two PTF materials are apparently higher than those in the PMC alloy. During partial remelting, the eutectic phases were dissolving towards the primary  $\alpha$ -Al particles, leading to an increase in the Mg and Si concentrations in the primary  $\alpha$ -Al particles and a decrease in the liquid. Under these conditions, the formed secondarily primary  $\alpha$ -Al grains should increase along with a decrease in the  $\text{Mg}_2\text{Si}$  based eutectic phases. It is worth noting that the Mg concentration in the PTF composite is slightly lower but the Si concentration is higher than those in the PTF alloy. This is due likely to the reactions of Mg and Al with  $\text{SiO}_2$  on the surfaces of oxidized  $\text{SiC}_p$  at high temperature (above 925 K [18]):  $3\text{SiO}_2(\text{s}) + 4\text{Al}(\text{l}) \rightarrow 2\text{Al}_2\text{O}_3(\text{s}) + 3\text{Si}(\text{s})$ ;  $\text{SiO}_2(\text{s}) + 2\text{Mg}(\text{l}) \rightarrow 2\text{MgO}(\text{s}) + \text{Si}(\text{s})$  and  $2\text{SiO}_2(\text{s}) + 2\text{Al}(\text{l}) + \text{Mg}(\text{l}) \rightarrow \text{MgAl}_2\text{O}_4(\text{s}) + 2\text{Si}(\text{s})$

**Table 1.** Compositions of the primary  $\alpha$ -Al particles or the grains of these materials.

Materials	Al (wt%)	Mg (wt%)	Si (wt%)
PMC alloy	99.6	0.3	0.1
PTF alloy	98.5	1.0	0.5
PTF composite	98.0	0.8	1.2

These reactions should reduce Mg concentration but enhance Si concentration in the liquid. Therefore, the diffusion of Mg atom from the liquid to the primary  $\alpha$ -Al particles decreased while that of the Si atom increased, resulting in a lower Mg concentration as well as higher Si concentration in the primary  $\alpha$ -Al particles of the PTF composite. Since Mg was a vital element to the formation of the eutectics during solidification, the eutectics amount in the PTF composite should be accordingly reduced. Summarily, the amount of  $\text{Mg}_2\text{Si}$  based eutectic phases in the PTF materials is distinctly less than that in the PMC alloy due to the dissolution of eutectic phases towards the primary  $\alpha$ -Al particles during partial remelting. The eutectics amount in PTF composite is slightly less than that in the PTF

alloy owing to the reactions of Mg and Al with  $\text{SiO}_2$  on the surfaces of oxidized  $\text{SiC}_p$  as well as the delayed microstructural evolution.

### 3.2. Porosity Evaluation

Figure 4 shows the typical SEM images of porosity distribution in these three materials under the same magnification. Representative pores can be easily identified in the PMC alloy, as presented in Figure 4a. Nevertheless, the pore amount in the PTF alloy is markedly reduced (Figure 4b) and the PTF composite is actually free of gases and shrinkage porosities (Figure 4c). The porosity percentage of the PTF alloy attains a value of 0.16% and the PTF composite is only 0.07% in comparison with that (3.50%) of the PMC alloy.

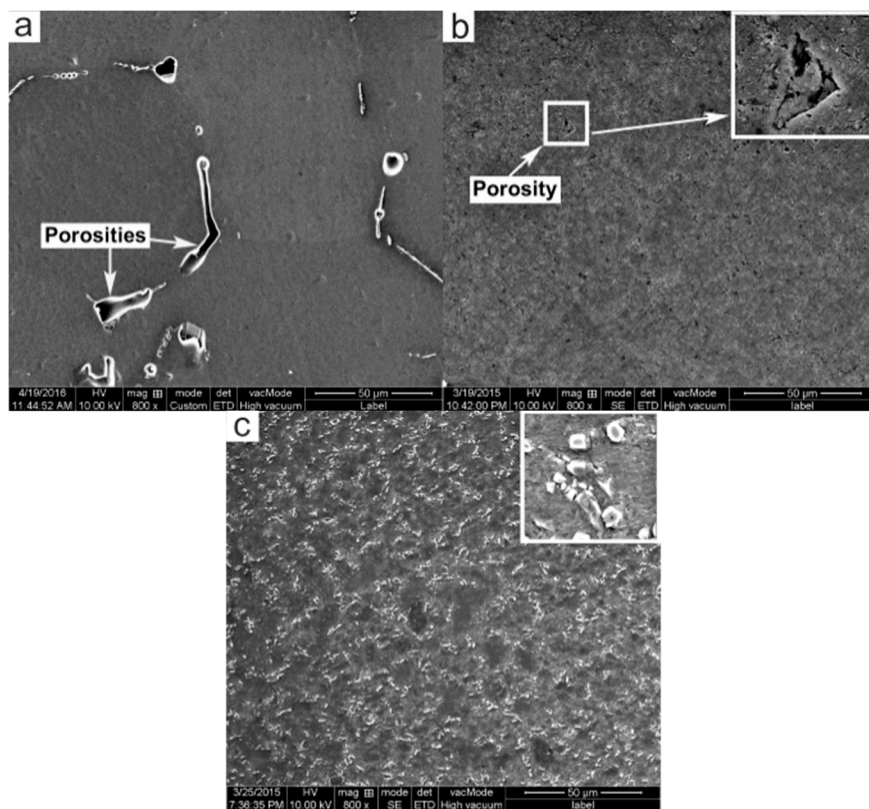
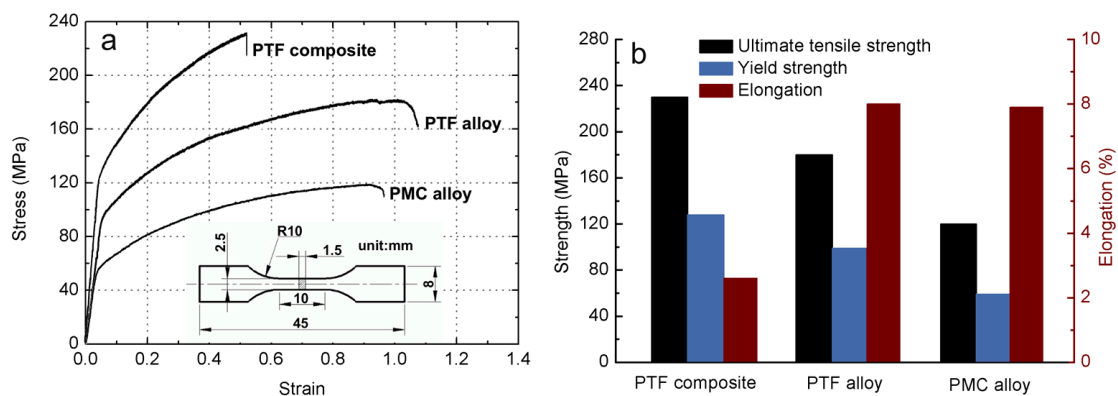


**Figure 4.** SEM images showing porosities in: (a) PMC-6061 alloy; (b) PTF-6061 alloy; (c) PTF- $\text{SiC}_p$ /6061Al composite.

The lower porosity of the PTF materials can be attributed to the following factors. First, a high pressure was applied in PTF during solidification, squeezing the liquid metal into the last solidified zone of the casting and consequently diminishing the shrinkage porosities. The ability to feed the solidification shrinkage is thereby improved. Besides, a relatively lower filling velocity was utilized during mold filling to effectively avoid air entrapment. The second one is due to the inherent characteristic of the semisolid forming [19–21]. The near-spheroidal morphology of the primary  $\alpha$ -Al particles in the PTF materials is more beneficial to liquid penetration for feeding [22]. Moreover, the proper liquid fraction of the PTF, which is lower than that of the PMC, should further decrease the probability of the shrinkage porosities as well as entrapped gases. It should be noted that the compactness of PTF composite is slightly higher than that of the PTF alloy. This is because the  $\text{SiC}_p$  in the secondarily solidified structures may likely fill in these intergranular pores and the pore amount in the PTF composite is therefore lower than that in the PTF alloy.

### 3.3. Tensile Properties

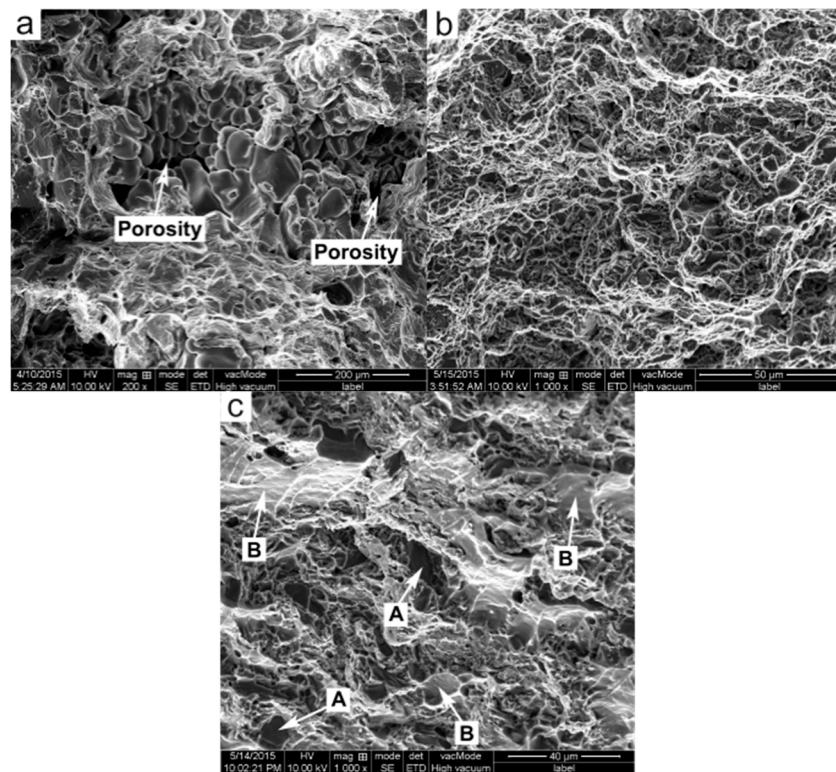
Figure 5 presents the mechanical properties of these three materials. It is evident that the ultimate tensile strength and yield strength of the PTF alloy are 180 MPa and 99 MPa, representing an enhancement of 50% and 67.8% respectively in comparison with those (120 MPa and 59 MPa) of the PMC alloy. Besides, the ultimate tensile strength and yield strength of the PTF composite attain the values of 230 MPa and 128 MPa, indicating an increase of 27.8% and 29.3%, respectively, in comparison with those of the PTF alloy. Nevertheless, the elongation of the PTF alloy attains the maximum value of 8.0% among these three materials. That is, the addition of  $\text{SiC}_p$  can significantly enhance the tensile strength but sacrifice the ductility. This is consistent with the results of many investigations on  $\text{SiC}_p/\text{Al}$  composites [23,24].



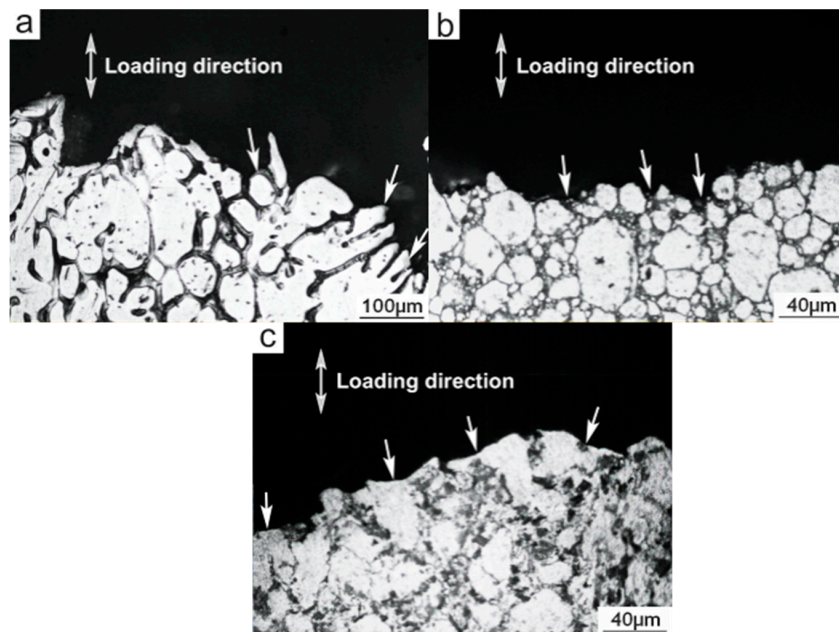
**Figure 5.** Tensile properties of these three materials: (a) stress-strain curves; (b) statistical results based on the average of minimum five tests.

The superior tensile properties of the PTF alloy than the PMC alloy can be attributed to the elimination of porosities and the decrease in the average grain size as mentioned above. In addition, the lower amount of  $\text{Mg}_2\text{Si}$  phase in the PTF alloy should also contribute to its superiority because  $\text{Mg}_2\text{Si}$  is detrimental to the tensile properties due to its brittle nature [25]. However, the superior tensile properties of the PTF composite than the PTF alloy should be primarily attributed to the existence of the  $\text{SiC}$  reinforcing particles to strengthen the  $\alpha\text{-Al}$  phase, and the detailed strengthening mechanisms will be quantitatively discussed in the following sections.

Figure 6 presents the typical fractographs of these three materials. The fracture surface of the PMC-6061 alloy is characterized by obvious porosity features (Figure 6a) and thus cracks preferentially originate in (marked by arrows in Figure 7a) and then propagate along the eutectic structures during tensile testing. In general, the fracture of the PMC alloy belongs to intergranular mode. In contrast, the microstructure of the fracture surface of the PTF-6061 alloy is quite compact. Accordingly, the porosity characteristics on the fracture surface of the PTF alloy disappear and are replaced by small dimples (Figure 6b). As mentioned above, thixoforming is effective in reducing or eliminating porosities and gas pores [10,16,19]. It is therefore feasible to give the PTF materials a high density. Differing from the PMC alloy, the fragile eutectic phases in the secondarily solidified structures become the weak points of the PTF alloy and thus cracks preferentially originate in and then develop along these phases in the process of tensile testing (marked by arrows in Figure 7b). Generally, the failure of the PTF alloy still belongs to the intergranular mode.



**Figure 6.** SEM fractographs of: (a) PMC-6061 alloy; (b) PTF-6061 alloy; (c) PTF-SiCp/6061Al composite.



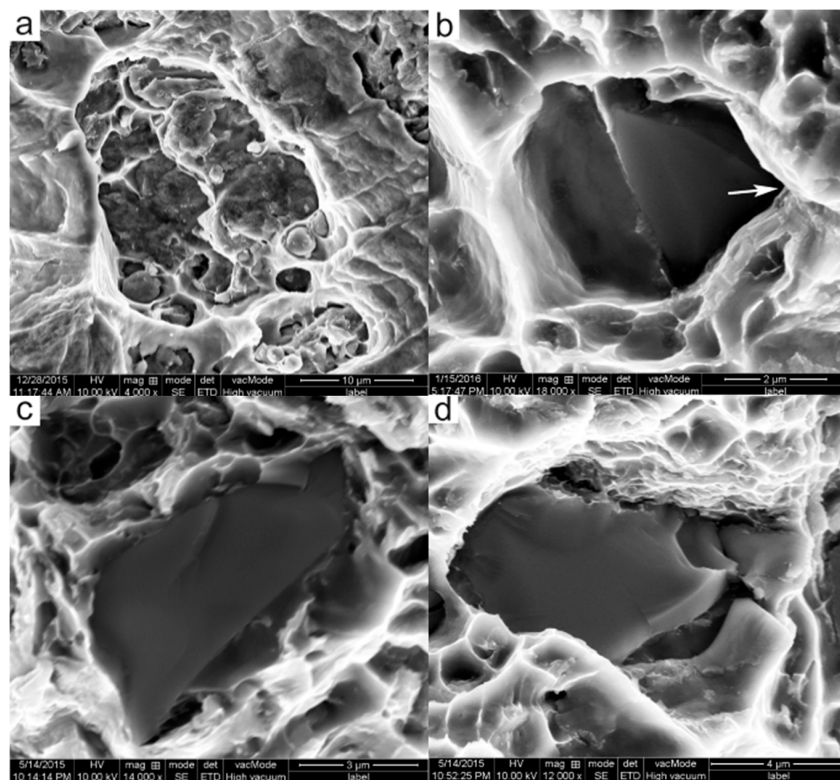
**Figure 7.** Side views of fracture surfaces of: (a) PMC-6061 alloy; (b) PTF-6061 alloy; (c) PTF-SiCp/6061 Al composite.

Figure 6c shows the fracture surface of the PTF-SiC<sub>p</sub>/6061 Al composite, which is characterized by visible SiC<sub>p</sub> (marked by arrows A) and flat facets (marked by arrows B). The microstructure of the fracture surface, similar to that of the PTF-6061 alloy, retains its compactness. Correspondingly, the dimple characteristics on the fracture surface of the PTF composite disappear and are substituted by flat facets induced by cracks moving through the primary  $\alpha$ -Al particles [19]. This accounts for the minimum elongation of the PTF composite in these three materials. The side view of the fracture

surface shows that the cracks propagate across the primary  $\alpha$ -Al particles (marked by arrows in Figure 7c) and the failure turns into the transgranular fracture mode. This change in the failure mode from intergranular (for the PTF alloy) to transgranular (for the PTF composite) is mainly due to the existence of  $\text{SiC}_p$  in the secondarily solidified structures, which generates a pinning effect against the crack propagation along the secondarily solidified structures during tensile testing. In summary, the fracture surface of the PMC-6061 alloy is characterized by porosity features while that of the PTF-6061 alloy is quite compact. Both of the fractures belong to the intergranular mode. The fracture surface of the PTF- $\text{SiC}_p$ /6061Al composite is characterized by visible  $\text{SiC}$  particles and flat facets. The failure turns into the transgranular fracture mode.

### 3.4. Strengthening Mechanisms of $\text{SiC}_p$

As mentioned above, the superior tensile strength of the PTF composite should be attributed to the existence of  $\text{SiC}$  reinforcing particles to strengthen the  $\alpha$ -Al phase. In effort to clarify the strengthening mechanisms of  $\text{SiC}_p$  in the PTF- $\text{SiC}_p$ /6061 Al composite, some typical fracture surfaces were observed under high magnification. Results from Figure 8 indicate that there are three kinds of fracture mode in the composites during tensile testing: ductile fracture across the matrix (Figure 8a) induced by the relatively lower matrix strength along with well bonded  $\text{SiC}_p$ /matrix interface and two types of failure correlated with  $\text{SiC}_p$ . One is the interfacial debonding of  $\text{SiC}_p$ /matrix (Figure 8b) and the other is the fragmentation of  $\text{SiC}_p$  (Figure 8c,d). It is thought that the interfaces of  $\text{SiC}_p$ /matrix are ascribed to an inherent interface because of the differences in the lattice constants and crystal structures [26]. Under this condition, local stress concentrations generate at the sharp edges and corners of the  $\text{SiC}_p$  in the process of tensile testing (marked by arrow in Figure 8b) and lead to the final debonding of  $\text{SiC}_p$ /matrix interfaces. The fragmentation of  $\text{SiC}_p$  includes two ways to fracture: either fractured parallel to the fractured surface (Figure 8c) or broken into several pieces (Figure 8d), which is also induced by the local stress concentrations generated in the  $\text{SiC}_p$ /matrix interface.



**Figure 8.** Typical SEM fractographs of the PTF- $\text{SiC}_p$ /6061Al composite. (a) fracture across the matrix; (b) debonding of the  $\text{SiC}_p$ /matrix interface; (c,d) fragmentation of the  $\text{SiC}_p$ .

The possible strengthening mechanisms that may operate in the PTF-SiC<sub>p</sub>/6061Al composite can be mainly divided into two categories: direct and indirect strengthening [27,28]. The direct strengthening, also known as the load transfer model, is based on the load sharing between the reinforcement and the matrix. The indirect strengthening is caused by the changes in the matrix microstructure due to the introduction of reinforcements, and the most used ones for the yield strength prediction of particle reinforced AMCs are Orowan strengthening and CTE mismatch [29–32]. To get a theoretical evaluation of the yield strength of present composite in the micromechanics approach, a simple linear summation of such terms is utilized [29,33,34]:

$$\sigma = \sigma_{cy} + \Delta\sigma_{or} + \Delta\sigma_{CTE} \quad (1)$$

As is indicated in Figure 8d, the SiC<sub>p</sub> have split into several parts and there are no obvious cracks in the surrounding matrix, revealing that the load transfer mechanism undoubtedly plays a role in strengthening the matrix. The most used load transfer model is the modified shear lag (MSL) model proposed by Nardon and Prewo [35]:

$$\sigma_{cy} = \sigma_{my} \left[ \frac{V_p (S + 2)}{2} + V_m \right] \quad (2)$$

where  $\sigma_{cy}$  is the composite yield strength,  $\sigma_{my}$  is the matrix yield strength,  $V_m$  and  $V_p$  are the volume fractions of matrix and reinforcing particles respectively,  $S$  is the average aspect ratio of the reinforcing particles.

For  $V_p + V_m = 1$ , Equation (2) can be substituted by

$$\sigma_{cy} = \sigma_{my} \left( 1 + \frac{V_p S}{2} \right) \quad (3)$$

Using the parameters listed in Table 2, Equation (3) can be rewritten as

$$\sigma_{cy} = 99 + 120.29V_p \quad (4)$$

**Table 2.** Parameters employed in the calculations (*m*: matrix; *p*: SiC<sub>p</sub>).

Parameter	Value
$G^m$ [36]	25.6 GPa
$b^m$ [29]	0.28 nm
$S$	2.43
$\Delta T$	640 K
$\alpha$ [37]	1.4
$C^m$ [29]	$23.6 \times 10^{-6} \text{ K}^{-1}$
$C^p$ [36]	$4.3 \times 10^{-6} \text{ K}^{-1}$

Figure 9 shows a good linear relationship between the yield strength increment and the particle volume fraction. As for the 10 vol% SiC<sub>p</sub>/6061Al composite employed in this work, the increment of yield strength  $\sigma_{cy}$  attains the value of 111 MPa.

The Orowan strengthening is induced by the interactions between the dispersed reinforcing particles and the dislocations due to the second-phase dispersions, precipitates and voids/cavities on the basis of the assumption that the spherical reinforcements ideally distribute uniformly in the matrix. The following expression is often used [37]

$$\Delta\sigma_{or} = \frac{2Gb}{0.6d\sqrt{2\pi/V_p}} \quad (5)$$

where  $\Delta\sigma_{or}$  is the yield strength increment brought about by the Orowan strengthening,  $G$  is the shear modulus of matrix,  $b$  is the Burgers vector and  $d$  is the average diameter of reinforcements. Putting the relevant parameters into Equation (5),  $\Delta\sigma_{or}$  can be expressed in terms of  $V_p$  by

$$\Delta\sigma_{or} = 1.3738\sqrt{V_p} \quad (6)$$

Figure 10 depicts the variations in the yield strength increments with the particle volume fractions on the basis of Equation (6). For the composite utilized in this work, the increment in yield strength  $\Delta\sigma_{or}$  assumes the value of only 0.43 MPa.

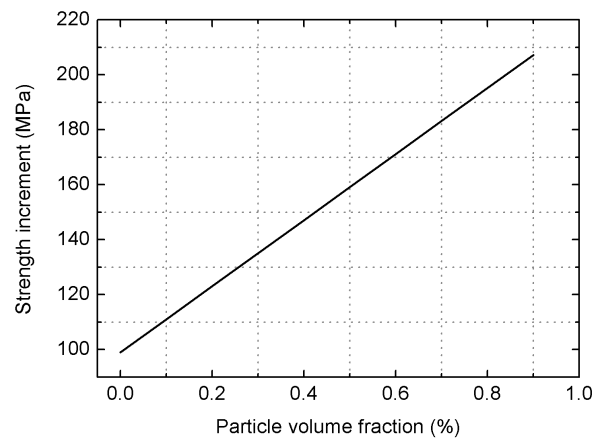


**Figure 9.** Dependence of the yield strength based on MSL model on the reinforcement volume fraction.

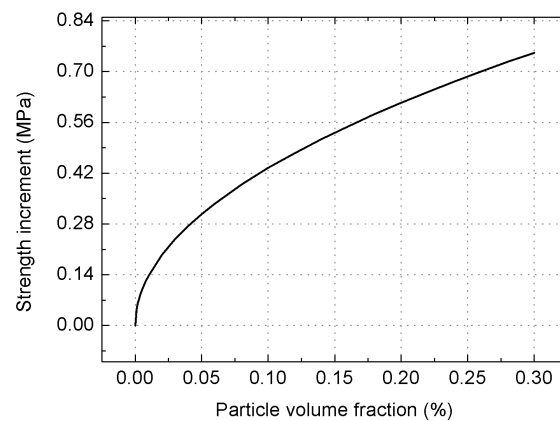


**Figure 10.** Dependence of the yield strength due to Orowan strengthening on the reinforcement volume fraction.

In addition, the CTE mismatch strengthening is caused by the dislocations resulting from the coefficient of thermal expansion mismatch between the matrix and the ceramic particles [32]. The resultant increment in the yield strength  $\Delta\sigma_{CTE}$  can be written as

$$\Delta\sigma_{CTE} = \alpha G b \sqrt{\rho} \quad (7)$$

where  $\alpha$  is the coefficient of dislocation strengthening and  $\rho$  is the dislocation density. It follows that

$$\rho = \frac{4V_p\Delta T\Delta C}{b(1-V_p)} \left( \frac{1}{t_1} + \frac{1}{t_2} + \frac{1}{t_3} \right) \quad (8)$$

where  $\Delta T$  is the temperature change from processing temperature to room temperature,  $\Delta C$  is the CTE difference between matrix and reinforcement particles, and  $t_1$ ,  $t_2$  and  $t_3$  are the thickness, width and length of reinforcements, respectively. With regard to the  $\text{SiC}_p$  employed in this paper, it was presumed that  $t_1 = t_2 = t_3 = 6.94 \mu\text{m}$ . Putting the values of these parameters into Equations (7) and (8),  $\Delta\sigma_{\text{CTE}}$  can be described by  $V_p$  as

$$\Delta\sigma_{\text{CTE}} = 85.61 \sqrt{\frac{V_p}{1 - V_p}} \quad (9)$$

Figure 11 shows the dependence of the yield strength increment on the particle volume fraction described by Equation (9), which shows that the increase in the particle volume fraction markedly enhances the yield strength increment. For the composite studied in this work, the increment in yield strength  $\Delta\sigma_{\text{CTE}}$  retains the value of 28.53 MPa.

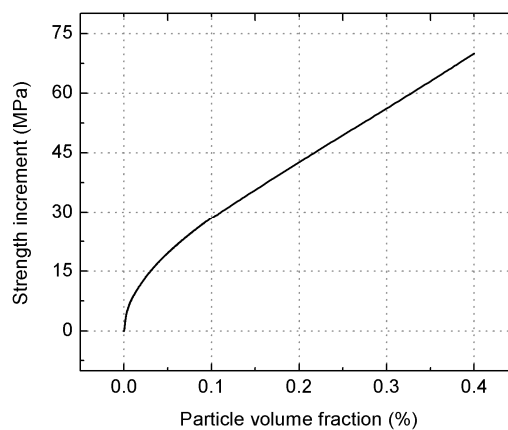


**Figure 11.** Dependence of the yield strength due to CTE mismatch on the reinforcement volume fraction.

From the discussions above, it is found that the direct strengthening due to the load transferring from the matrix to the reinforcements plays the largest role in improving the yield strength. However, the strength increase obtained from the Orowan strengthening is quite minor. This is mainly attributed to the micro size of the employed  $\text{SiC}_p$  and the large inter-particle spacing [12]. Substituting the aforementioned Equations (4), (6) and (9) into Equation (1), it follows that

$$\sigma = 99 + 120.29V_p + 1.3738\sqrt{V_p} + 85.61\sqrt{\frac{V_p}{1 - V_p}} \quad (10)$$

The yield strength of the current PTF- $\text{SiC}_p$ /6061Al composite calculated through Equation (10) is 140 MPa, which is apparently higher than the experimental data (128 MPa). This result, as reported by Chen *et al.* [37], can be primarily attributed to the neglect of the influence of the  $\text{SiC}_p$  failure (including  $\text{SiC}_p$ /matrix debonding and  $\text{SiC}_p$  cracking) on the composite's yield strength. As the failed  $\text{SiC}_p$  cannot effectively bear load, a decrease in the yield strength will inevitably appear. Considering these factors, a modified model taking into account the  $\text{SiC}_p$  failure fraction  $f$  is proposed

$$\sigma = 99 + 120.29V_p(1 - f) + 1.3738\sqrt{V_p(1 - f)} + 85.61\sqrt{\frac{V_p(1 - f)}{1 - V_p(1 - f)}} \quad (11)$$

In accordance with the authors' previous study [12], the failure fraction  $f$  attains the value of 25.6%. Substituting this value into Equation (11), the calculated yield strength for the present composite is 132.6 MPa, which is much closer to the experimental data (128 MPa). Therefore, this model in the form of Equation (11) accurately captures the strengthening mechanisms and discloses the significant

effects of  $\text{SiC}_p$  failure including  $\text{SiC}_p$ /matrix debonding and  $\text{SiC}_p$  cracking on the yield strength of the PTF- $\text{SiC}_p$ /6061Al composite.

#### 4. Conclusions

1. The microstructure of the PMC-6061 alloy is composed of coarse and equiaxed  $\alpha$  dendrites with an average size of 90.01  $\mu\text{m}$  and interdendritic net-like eutectic phases, but the microstructure of the PTF- $\text{SiC}_p$ /6061Al composite, similar to that of the PTF-6061 alloy, consists of near-spheroidal primary particles and intergranular secondarily solidified structures except  $\text{SiC}_p$ , which are distributed in the secondarily solidified structures.
2. The primary particles of the PTF composite are more irregular and the amount of secondarily solidified structures is lower than those of the PTF alloy because of the delayed microstructural evolution rate during partial remelting. Besides, the size of the primary particles is slightly smaller than that in the PTF alloy due to the delayed microstructural evolution rate as well as the pinning effect of  $\text{SiC}_p$  against the coalescence of the nearby primary particles.
3. The amount of  $\text{Mg}_2\text{Si}$  based eutectic phases in the PTF materials is distinctly lower than that in the PMC alloy due to the dissolution of eutectic phases towards the primary  $\alpha$ -Al particles during partial remelting. The eutectics amount in PTF composite is slightly lower than that in the PTF alloy owing to the reactions of Mg and Al with  $\text{SiO}_2$  on the surfaces of oxidized  $\text{SiC}_p$  as well as the delayed microstructural evolution.
4. The microstructures of the PTF materials are quite compact while that of the PMC alloy is porous. The porosity elimination in the PTF materials is due to the applied high pressure during solidification, the low filling velocity during mold filling, the improved feeding ability of near-spheroidal primary  $\alpha$ -Al particles and the low liquid fraction of the semisolid slurry.
5. The ultimate tensile strength and the yield strength of the PTF composite are 230 MPa and 128 MPa, which is apparently higher than those of the PTF (180 MPa and 99 MPa) and PMC (120 MPa and 59 MPa) alloys. The elongation of the PTF alloy attains the maximum value of 8.0% among these three materials.
6. The superior tensile properties of the PTF alloy than the PMC alloy can be attributed to the elimination in porosities and the decrease in the average grain size as well as the lower amount of  $\text{Mg}_2\text{Si}$  phase in the former alloy. The superior tensile properties of the PTF composite over the PTF alloy should be attributed to the existence of the SiC reinforcing particles to strengthen the  $\alpha$ -Al phase.
7. The fracture surface of the PMC-6061 alloy is characterized by porosity features while that of the PTF-6061 alloy is quite compact. Both of the fractures belong to the intergranular mode. The fracture surface of the PTF- $\text{SiC}_p$ /6061Al composite is characterized by visible SiC particles and flat facets. The failure turns into the transgranular fracture mode.
8. The strength increment resulted from MSL model plays largest role in improving the yield strength of the composite. However, the strength increase obtained from the Orowan strengthening is quite minor owing to the micro size of the employed  $\text{SiC}_p$  and the large inter-particle spacing.
9. A modified model taking into consideration the  $\text{SiC}_p$  failure fraction was proposed to calculate the yield strength of the PTF composite. The obtained theoretical results were quite consistent with the experimental data, revealing that the  $\text{SiC}_p$  failure including  $\text{SiC}_p$ /matrix debonding and  $\text{SiC}_p$  cracking has a significant effect on the composite's yield strength.

**Acknowledgments:** The authors wish to express thanks for financial support from the Basic Scientific Fund of Gansu Universities (Grant No. G2014-07), the Program for New Century Excellent Talents in University of China (Grant No. NCET-10-0023) and the Program for Hongliu Outstanding Talents of Lanzhou University of Technology (Grant No. 2012-03).

**Author Contributions:** Xuezheng Zhang did the experiments, data analysis and wrote the paper. Tijun Chen reviewed and revised the manuscript of this paper. He Qin; and Chong Wang contributed to the data analysis.

**Conflicts of Interest:** The authors declare no conflict of interest.

## References

1. Liu, Z.Y.; Xiao, B.L.; Wang, W.G.; Ma, Z.Y. Elevated temperature tensile properties and thermal expansion of CNT/2009Al composites. *Compos. Sci. Technol.* **2012**, *72*, 1826–1833. [[CrossRef](#)]
2. Sajjadi, S.A.; Ezatpour, H.R.; Beygi, H. Microstructure and mechanical properties of Al–Al<sub>2</sub>O<sub>3</sub> micro and nano composites fabricated by stir casting. *Mater. Sci. Eng. A* **2011**, *528*, 8765–8771. [[CrossRef](#)]
3. Hamedan, A.D.; Shahmiri, M. Production of A356-1 wt% SiC nanocomposite by the modified stir casting method. *Mater. Sci. Eng. A* **2012**, *556*, 921–926. [[CrossRef](#)]
4. Lan, J.; Yang, Y.; Li, X. Microstructure and microhardness of SiC nanoparticles reinforced magnesium composites fabricated by ultrasonic method. *Mater. Sci. Eng. A* **2004**, *386*, 284–290. [[CrossRef](#)]
5. Onat, A.; Akbulut, H.; Yilmaz, F. Production and characterisation of silicon carbide particulate reinforced aluminium–copper alloy matrix composites by direct squeeze casting method. *J. Alloys Compd.* **2007**, *436*, 375–382. [[CrossRef](#)]
6. Hsu, C.W.; Chao, C.G. Effect of heat treatments on In-Situ Al<sub>2</sub>O<sub>3</sub> /TiAl<sub>3</sub> composites produced from squeeze casting of TiO<sub>2</sub> /A356 composites. *Metall. Mater. Trans. B* **2002**, *33*, 31–40. [[CrossRef](#)]
7. Chao, Y.; He, F.H.; de los Reyes, M.; Long, Y.; Zhou, X.-T.; Xia, T.; Zhang, D.-L. Microstructures and Tensile Properties of Ultrafine-Grained Ni–(1–3.5) wt% SiCNP Composites Prepared by a Powder Metallurgy Route. *Acta Metall. Sin. Engl. Lett.* **2015**, *7*, 809–816.
8. Ogel, B.; Gurbuz, R. Microstructural characterization and tensile properties of hot pressed Al–SiC composites prepared from pure Al and Cu powders. *Mater. Sci. Eng. A* **2001**, *301*, 213–220. [[CrossRef](#)]
9. Li, P.; Chen, T.; Zhang, S.; Guan, R. Research on Semisolid Microstructural Evolution of 2024 Aluminum Alloy Prepared by Powder Thixoforming. *Metals* **2015**, *5*, 547–564. [[CrossRef](#)]
10. Chen, Y.S.; Chen, T.J.; Zhang, S.Q.; Pu-Bo, L.I. Effects of processing parameters on microstructure and mechanical properties of powder-thixoforged 6061 aluminum alloy. *Trans. Nonferrous Met. Soc. China* **2015**, *25*, 699–712. [[CrossRef](#)]
11. Chen, Y.S.; Chen, T.J.; Fu, W.; Li, P.B. Microstructural Evolution during Partial Remelting of 6061 Aluminum Bulk Alloy Prepared by Cold-Pressing of Alloy Powder. *Adv. Mater. Res.* **2013**, *7*, 20–24. [[CrossRef](#)]
12. Zhang, X.Z.; Chen, T.J.; Qin, Y.H. Effects of solution treatment on tensile properties and strengthening mechanisms of SiCp/6061 Al composites fabricated by powder thixoforming. *Mater. Des.* **2016**, *99*, 182–192.
13. Li, P.B.; Chen, T.J.; Zhang, S.Q.; Wang, Y.J. Effects of partial remelting on the microstructure evolution of SiCp/2024p aluminum composites prepared by alloy powder cold pressing. *Spec. Cast. Nonferrous Alloys* **2015**, *35*, 260–263.
14. Chen, Y.S. The Research on Microstructure and Mechanical Properties of SiCp/6061 Al Matrix Composite Prepared by Powder Thixoforming. Master's Thesis, Lanzhou University of Technology, Lanzhou, China, 20 April 2014.
15. Belov, N.A.; Eskin, D.G.; Aksenov, A.A. *Multicomponent Phase Diagrams: Applications for Commercial Aluminum Alloys*; Elsevier: Amsterdam, The Netherlands, 2005.
16. Cheng, F.L.; Chen, T.J.; Qi, Y.S.; Zhang, S.Q.; Yao, P. Effects of solution treatment on microstructure and mechanical properties of thixofomed Mg<sub>2</sub>Si<sub>p</sub>/AM60B composite. *J. Alloys Compd.* **2015**, *636*, 48–60. [[CrossRef](#)]
17. Chen, T.; Jiang, X.; Huang, H.; Ma, Y.; Li, Y.; Hao, Y. Semisolid Microstructure of AZ91D Magnesium Alloy Refined by MgCO<sub>3</sub>. *Int. J. Met.* **2012**, *6*, 43–54. [[CrossRef](#)]
18. Mitra, R.; Rao, V.S.C.; Maiti, R.; Chakraborty, M. Stability and response to rolling of the interfaces in cast Al–SiC<sub>p</sub> and Al–Mg alloy–SiC<sub>p</sub> composites. *Mater. Sci. Eng. A* **2004**, *379*, 391–400. [[CrossRef](#)]
19. Zhang, S.; Chen, T.; Cheng, F.; Li, P. A Comparative Characterization of the Microstructures and Tensile Properties of As-Cast and Thixoforged *in situ* AM60B-10 vol% Mg<sub>2</sub>Si<sub>p</sub> Composite and Thixoforged AM60B. *Metals* **2015**, *5*, 457–470. [[CrossRef](#)]
20. Flemings, M.C. Solidification processing. *Metall. Mater. Trans. A* **1974**, *5*, 2121–2134. [[CrossRef](#)]

21. Fan, Z.; Fang, X.; Ji, S. Microstructure and mechanical properties of rheo-diecast (RDC) aluminium alloys. *Mater. Sci. Eng. A* **2005**, *412*, 298–306. [[CrossRef](#)]
22. Burt, D.J. Direct thermal method: New process for development of globular alloy microstructure. *Int. J. Cast. Met. Res.* **2003**, *16*, 418–426.
23. Tan, M.; Xin, Q.; Li, Z.; Zong, B.Y. Influence of SiC and Al<sub>2</sub>O<sub>3</sub> particulate reinforcements and heat treatments on mechanical properties and damage evolution of Al-2618 metal matrix composites. *J. Mater. Sci.* **2001**, *36*, 2045–2053. [[CrossRef](#)]
24. Song, M. Effects of volume fraction of SiC particles on mechanical properties of SiC/Al composites. *Trans. Nonferrous Met. Soc. China* **2009**, *19*, 1400–1404. [[CrossRef](#)]
25. Chen, T.; Zhang, S.; Chen, Y.; Li, Y.; Ma, Y.; Hao, Y. Effects of Reheating Duration on the Microstructures and Tensile Properties of Thixoforged In Situ Mg<sub>2</sub>Si<sub>p</sub>/AM60B Composites. *Acta. Metall. Sin.* **2014**, *27*, 957–967. [[CrossRef](#)]
26. Gubicza, J.; Nauyoks, S.; Balogh, L.; Labar, J.; Zerda, T.W.; Ungár, T. Influence of sintering temperature and pressure on crystallite size and lattice defect structure in nanocrystalline SiC. *J. Mater. Res.* **2007**, *22*, 1314–1321. [[CrossRef](#)]
27. Zhang, Q.; Xiao, B.L.; Wang, W.G.; Ma, Z.Y. Reactive mechanism and mechanical properties of *in situ* composites fabricated from an Al–TiO<sub>2</sub> system by friction stir processing. *Acta Mater.* **2012**, *60*, 7090–7103. [[CrossRef](#)]
28. Wang, Z.; Prashanth, K.G.; Scudino, S.; Chaubey, A.K.; Sordelet, D.J.; Zhang, W.W.; Li, Y.Y.; Eckert, J. Tensile properties of Al matrix composites reinforced with in-situ devitrified Al<sub>84</sub>Gd<sub>6</sub>Ni<sub>7</sub>Co<sub>3</sub> glassy particles. *J. Alloys Compd.* **2013**, *586*, S419–S422. [[CrossRef](#)]
29. Wang, Z.; Tan, J.; Sun, B.A.; Scudino, S.; Prashanth, K.G.; Zhang, W.W.; Li, Y.Y.; Eckert, J. Fabrication and mechanical properties of Al-based metal matrix composites reinforced with Mg<sub>65</sub>Cu<sub>20</sub>Zn<sub>5</sub>Y<sub>10</sub> metallic glass particles. *Mater. Sci. Eng. A* **2014**, *4*, 53–58. [[CrossRef](#)]
30. Poirier, D.; Drew, R.A.L.; Trudeau, M.L.; Gauvin, R. Fabrication and properties of mechanically milled alumina/aluminum nanocomposites. *Mater. Sci. Eng. A* **2010**, *527*, 7605–7614. [[CrossRef](#)]
31. Yan, S.J.; Dai, S.L.; Zhang, X.Y.; Yang, C.; Hong, Q.H.; Chen, J.Z.; Lin, Z.M. Investigating aluminum alloy reinforced by graphene nanoflakes. *Mater. Sci. Eng. A* **2014**, *612*, 440–444. [[CrossRef](#)]
32. Rashad, M.; Pan, F.; Tang, A.; Asif, M. Effect of Graphene Nanoplatelets addition on mechanical properties of pure aluminum using a semi-powder method. *Prog. Nat. Sci. Mater. Int.* **2014**, *3*, 101–108. [[CrossRef](#)]
33. Tabandeh-Khorshid, M.; Ferguson, J.B.; Schultz, B.F.; Kim, C.S.; Cho, K.; Rohatgi, P.K. Strengthening mechanisms of graphene and Al<sub>2</sub>O<sub>3</sub> reinforced aluminum nanocomposites synthesized by room temperature milling. *Mater. Des.* **2015**, *92*, 79–87. [[CrossRef](#)]
34. Tong, X.C.; Ghosh, A.K. Fabrication of *in situ* TiC reinforced aluminum matrix composites. *J. Mater. Sci.* **2001**, *36*, 4059–4069. [[CrossRef](#)]
35. Nardone, V.C.; Prewo, K.M. On the strength of discontinuous silicon carbide reinforced aluminum composites. *Scr. Metall.* **1986**, *20*, 43–48. [[CrossRef](#)]
36. Min, S.; Xie, C.Q.; He, Y.-H. Model of effects of particle failure on yield stress of SiC reinforced aluminum alloy composites. *J. Nonferrous Met.* **2010**, *20*, 244–249.
37. Chen, K.H.; Fang, L.; Li, X.; Huang, D.W.; Fang, H.C. Influence of particle failure on strength of SiCp/Al composite. *J. Cent. South Univ. Sci. Technol.* **2008**, *39*, 493–499.

